

Size and Morphology of Suspended WO_3 Particles Control Photochemical Charge Carrier Extraction and Photocatalytic Water Oxidation Activity

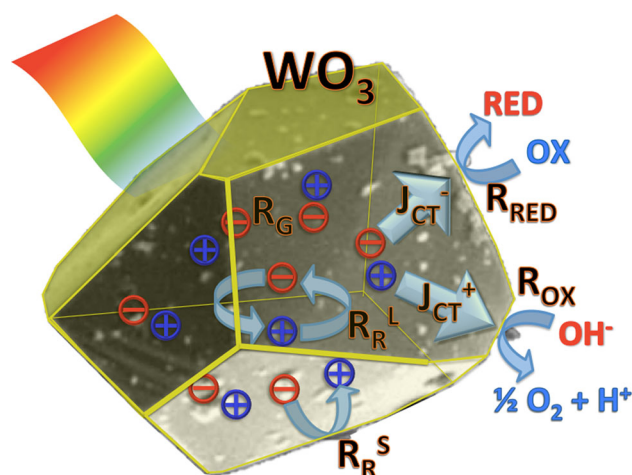
Kathryn A. Newton¹ · Frank E. Osterloh¹

© Springer Science+Business Media New York 2016

Abstract Tungsten(VI) oxide (WO_3) is a robust n-type semiconductor with a 2.7 eV bandgap and proven activity for photoanodic water oxidation in the context of tandem water splitting photocatalysis. Here we present a systematic investigation of three types of WO_3 particles to determine the influence of particle size and morphology on photocatalytic oxygen evolution, optical properties, energetics, and photocurrent generation. Nanodots (32 ± 16 nm), nanoplates (476 ± 98 nm by 58 ± 16 nm), and WO_3 microcrystals (~ 2 μm) for the study were synthesized by calcination of WO_3 powders or by hydrolysis of Na_2WO_4 , followed by calcination. All samples crystallize in the monoclinic rhenium trioxide structure type and have band gaps between 2.75 and 2.87 eV. From 0.01 M aqueous NaIO_4 under 610 mW cm^{-2} visible illumination (>400 nm), 30 mg of the WO_3 dots, plates, and microcrystals evolve oxygen at 31.6, 16.5, and 2.9 $\mu\text{mol h}^{-1}$, respectively. Photoelectrochemistry on WO_3 particle films in aqueous K_2SO_4 at pH 3.5 confirms decreasing anodic photocurrents (25, 17.8, and 7.7 $\mu\text{A cm}^{-2}$, respectively, at +1.0 V NHE) with decreasing particles size, and similar photoonset potentials of +0.25 V vs. NHE for all samples. This suggests that the photocatalytic activity differences among the WO_3 series are controlled not by the energetics but by the kinetics of minority and majority carrier transport within the particles. The reactivity trends can be

quantitatively described with the one-dimensional continuity model for charge generation, recombination, and transport.

Graphical Abstract



Keywords Solar fuel · Fermi level · Minority carrier diffusion length · Water splitting · Sodium iodate

1 Introduction

As a special form of artificial photosynthesis, the water splitting reaction holds great potential within the context of a sustainable energy economy [1–3]. Because of its stability and its visible light responsive band gap ($E_G = 2.7$ eV), WO_3 has long been a material of interest for photoelectrochemical water oxidation [4–13], and more recently as a component in suspended tandem photocatalysts [14–19]. Besides doping [20] and derivatization with

Electronic supplementary material The online version of this article (doi:10.1007/s11244-016-0549-3) contains supplementary material, which is available to authorized users.

✉ Frank E. Osterloh
fosterloh@ucdavis.edu

¹ Department of Chemistry, University of California, Davis,
One Shields Avenue, Davis, CA 95616, USA

cocatalysts [21, 22], nanoscaling has been used to increase the performance of WO_3 for light driven water oxidation [9, 23–25]. Reducing the size of absorber particles not only promotes charge carrier extraction [26, 27], but can also lead to quantum size effects [9], stronger electrolyte screening [28], and reduced internal electric fields [2, 3]. Most studies on particle size effects have focused on WO_3 photoelectrodes. For example, Augustynski and coworkers reported that during photoelectrochemical methanol oxidation, nanostructured WO_3 electrodes possess enhanced visible light absorption and current [10, 12]. Photoanodic water oxidation with photocurrents of $2.7\text{--}3.8\text{ mA cm}^{-2}$, depending on illumination conditions and bias, can be achieved as a result of improved minority carrier injection into the solution [29, 30]. For suspended WO_3 particles, the literature on scaling effects is more sparse [31], and the relation between particle size and photocatalytic water oxidation activity is less clear. In 2009, Hong et al. reported that larger WO_3 particles showed higher photoactivity for water oxidation with AgNO_3 as acceptor because of a well-developed space charge layer and high crystallinity. They also reported that for photoelectrochemical water oxidation, smaller crystals performed better because of reduced hole diffusion length [32]. On the other hand, in 2013 Amano et al. found that the water oxidation activity of WO_3 with AgNO_3 as sacrificial acceptor *increased* with particle size for spherical diameters smaller than 200 nm because surface recombination was suppressed in the larger particles [33]. To shed further light on the particle size issue, we have performed a systematic study on photocatalytic oxygen evolution with both suspended WO_3 particles and particulate film electrodes, in the presence of a strong chemical bias, sodium meta-periodate (NaIO_4). We find that the O_2 evolution activity among three different WO_3 samples increases with smaller particle size and also depends on particle morphology. Photoelectrochemical measurements and a one-dimensional continuity analysis [34, 35] reveal that the trend can be attributed to the differing pathlengths for electron and hole transport in the particles.

2 Experimental Section

2.1 Material Synthesis

Tungsten(VI) oxide nanocrystals were synthesized using a cation exchange method [36, 37]. A column was loaded with 15 mL cation exchange resin (Dowex[®] 50, 20–50 Mesh, J. T. Baker Chemical Co. Lot: 521731), which had been prepared by soaking in 1 M H_2SO_4 . The loaded

column was rinsed with 30 mL 18 M Ω water, and 5 mL of 0.05 M $\text{Na}_2\text{WO}_4 \cdot 2\text{H}_2\text{O}$ (aq) (99 %, Acros Organics Lot: AO3179265) was washed through the column with 30 mL 18 M Ω water. The eluted solution was collected in three fractions; the yellow middle fraction was collected in 20 mL ethanol under stirring [11]. To make 30 nm particles (nanodots), polyethylene glycol (FW 8000, Sigma Lot: 121F0225) was added to the solution in a 2:1 mass ratio with the WO_3 . The resulting yellow solution was aged overnight, dried at 110 °C for 2 h, and then annealed at 500 °C for 1.5 h in a furnace. To synthesize nanoplates, PEG-8000 was omitted from the procedure. Again, the resulting yellow solution was aged overnight, then air-dried at 110 °C for 2 h, and annealed at 500 °C for 1.5 h in a tube furnace. Microcrystalline WO_3 was obtained by annealing commercial WO_3 (99+ %, Acros Organics Lot: A0272018) at 1000 °C for 5 h. The solid was then suspended in 18 M Ω water by brief sonication. Larger particles were allowed to settle and were collected after decanting the supernatant. Smaller particles remained suspended and were disposed of with the supernatant. The larger particles were re-suspended and isolated two more times to obtain pure microcrystals [38]. NaIO_4 (98 % pure) for the photocatalytic tests was purchased from Alfa Aesar and recrystallized once from water before use.

2.2 Preparation of Films

Films used for diffuse reflectance spectroscopy, electrochemistry, and scanning electron microscopy were prepared on conductive fluorine-doped tin oxide (FTO) (TEC 15, MTI Corporation, 12–14 Ω) and Au–Glass substrates (Thermo Scientific). FTO substrates were prepared by successive 15 min sonications in acetone (Sigma Aldrich, HPLC Grade, $\geq 99\%$), methanol (Sigma Aldrich, $\geq 99.8\%$) and 2-propanol (Fisher Scientific, HPLC Grade, 99.9 %). Au–glass substrates were prepared by rinsing with acetone followed by soaking for 15 min in a solution of 0.1 M KOH in 30 % hydrogen peroxide. Films were made by suspending WO_3 in 18 M Ω water (acidified with 0.5 M nitric acid) and drop-coating 0.1 mL of suspension over a 1 cm² area. Films were air-dried overnight and then annealed at 450 °C for 1 h to improve contact between the deposited material and the conductive substrates. The film thickness was controlled with the concentration of the WO_3 suspensions. Films were made using 2 mg mL⁻¹ suspension for diffuse reflectance (DRS) UV–Vis measurements and 5 mg mL⁻¹ for electrochemical experiments. Film thickness was measured using a Veeco Dektak profilometer.

2.3 Characterization

Powder X-ray diffraction studies confirmed the monoclinic crystal structure of the nanodots, nanoplates, and microcrystals. X-ray patterns were collected on a Rigaku Mini-Flex 600, which is equipped with a Cu X-ray source ($\lambda = 1.5418 \text{ \AA}$) and a D/teX Ultra high-speed silicon strip detector with K_{β} filter. The sample was prepared on a Si(510) single-crystal, zero-background holder and was rotated at 60 rpm during collection. The pattern was collected from 10° to $90^{\circ} 2\theta$ in continuous sweep mode at a rate of $7.5^{\circ} 2\theta \text{ min}^{-1}$ with a step size of $0.02^{\circ} 2\theta$. Results of a Scherrer size analysis are shown in Table S1.

Sample morphologies were examined using scanning electron microscopy (SEM) and transmission electron microscopy (TEM). SEM images were obtained on a FEI LX30 high-resolution scanning electron microscope at operating voltages of 5–15 kV. TEM images were taken with a Phillips CM-12 transmission electron microscope with an accelerating voltage of 120 kV. TEM samples were prepared by drop-casting dilute particle dispersions onto carbon-coated copper grids and allowing to air-dry. Particle sizes were determined from electron micrographs using Image-J software.

Photoelectrochemical measurements were performed on WO_3 films on an FTO working electrode with a platinum wire counter electrode and a saturated calomel electrode (SCE) as reference. Electrodes were connected to a Gamry Reference 600 potentiostat, controlled by a PC. The cell was calibrated to the potential of the potassium hexacyanoferrate(III/II) redox couple ($E = +0.358 \text{ V}$ vs. NHE). Potentials were swept (10 mV s^{-1}) from negative to positive potentials for dark scans and (10 mV s^{-1}) from positive to negative potentials for illuminated and chopped light scans. The cell was constructed in a quartz flask and was illuminated by a 300 W Xe lamp or by a 435 nm (blue) LED. All experiments were conducted using 0.1 M K_2SO_4 (pH 3.5) as the electrolyte or 0.1 M K_2SO_4 in 20 % methanol and water (pH 3.5) electrolyte solution [20, 39, 40]. The cell was purged with nitrogen gas prior to measurements to remove air.

Diffuse reflectance UV–Vis spectra were collected using a Thermo Scientific Evolution 220 UV–Vis Spectrophotometer, equipped with an integrating sphere. Collected reflectance data was converted to Kubelka–Munk absorbance by the equation $f(R) = (1 - R)^2(2R)^{-1}$. Absorbance is reported as a function of wavelength of incident light and was used to generate Tauc Plots using the relationship $E(\text{eV}) = (h\nu \times f(R))^{\frac{1}{n}}$, with $n = \frac{1}{2}$ for allowed direct transitions and $n = 2$ for allowed indirect transitions. Band gap transitions were estimated using the line tangent at the inflection point of the plot.

2.4 Photocatalytic Tests

Oxygen evolution experiments were conducted using 30 mg samples of WO_3 catalyst, suspended in 80 mL of aqueous 0.01 M NaIO_4 solution acidified to pH 3.2–3.3 with dilute HNO_3 in a 127 mL quartz flask. Prior to irradiation, the filled flask was evacuated to ~ 20 Torr under vigorous stirring and was refilled with argon. This process was repeated four more times. Suspensions were irradiated for 5 h under continuous stirring by a 300 W Xe lamp ($\sim 610 \text{ mW cm}^{-2}$ at the flask surface), equipped with a 0.22 M aqueous NaNO_2 infrared and long-pass filter ($>400 \text{ nm}$). The gas composition of the headspace was measured every hour using a Varian gas chromatograph equipped with a Supelco molecular 80/60 sieve 5A column, a thermal conductivity (TCD) detector, and argon carrier gas.

3 Results and Discussion

Powder X-ray diffraction patterns confirm that all WO_3 samples are phase-pure in the monoclinic ReO_3 crystal structure type (Fig. S1). According to electron micrographs WO_3 nanodots are round particles with an average diameter of $32 \pm 16 \text{ nm}$ (Fig. 1). WO_3 nanoplates are square plate-like particles with dimensions of $476 \pm 98 \text{ nm}$ by $58 \pm 16 \text{ nm}$. WO_3 microcrystals (Figs. 1c, S2) are $2 \mu\text{m}$ thick on average and have irregular morphology. The size of the dots is similar to the diameter from the Scherrer equation (21.6–24.2 nm in Table S1), supporting the presence of single crystals in this case. For the nanoplates, the Scherrer analysis (27.8–31.5 nm) suggests the presence of multidomain crystals.

All samples have the characteristic yellow color of WO_3 and similar absorption onset near 450 nm, according to diffuse reflectance spectra (Fig. 2). From Tauc plots (Fig. S3) the direct band gaps were determined as 2.75 eV for the nanodots, 2.87 eV for the nanoplates, and 2.80 eV for the microcrystals. The indirect band gaps followed the same trend and were about 0.15 eV smaller. These values compare well with literature for bulk particles and nanoparticles made by similar syntheses [11, 41].

In order to determine the effect of particle size on catalytic oxygen evolution, 30 mg of each sample was suspended in 80 mL of 0.01 M NaIO_4 (aq) at pH 3.5. NaIO_4 is a strong oxidizing agent with a standard reduction potential of +1.40 V at pH 3.5 [42]. It was chosen instead of the more commonly used NaIO_3 , because the latter requires a co-catalyst with WO_3 for water oxidation [43], which would have made it difficult to probe the intrinsic activity of WO_3 particles. Based on control experiments (Fig. S4), only small amounts of O_2 were evolved when a 0.01 M

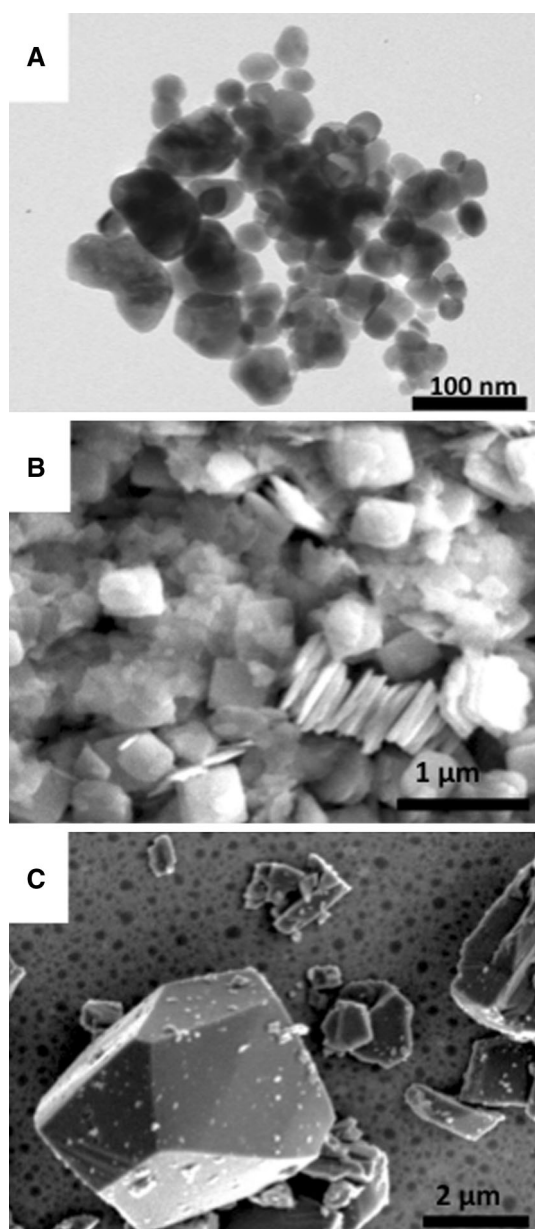


Fig. 1 TEM images of **a** WO_3 nanodots and SEM images of **b** WO_3 nanoplates, and **c** WO_3 microcrystals

NaIO_4 (aq) solution at pH 3.5 was irradiated without catalyst ($<4 \mu\text{mol O}_2$ after 5 h) or when 30 mg of catalyst in 0.01 M NaIO_4 (aq) at pH 3.5 were heated to 50°C in the dark ($<6 \mu\text{mol O}_2$ after 5 h). This confirms the majority of evolved O_2 in the $\text{WO}_3/\text{NaIO}_4$ system to be from a photocatalytic process. Also, to ensure that NaIO_4 was not rate limiting, its concentration was adjusted to 0.01 M through empirical variation experiments (Fig. S4b).

Figure 3a shows O_2 evolution from the three types of WO_3 particles under visible light ($>400 \text{ nm}$) at pH 3.5. All samples evolved oxygen linearly over 5 h. The oxygen evolution rate was particle size dependent and decreased from $31.63 \mu\text{mol h}^{-1}$ for the nanodots, to $16.48 \mu\text{mol h}^{-1}$ for the nanoplates,

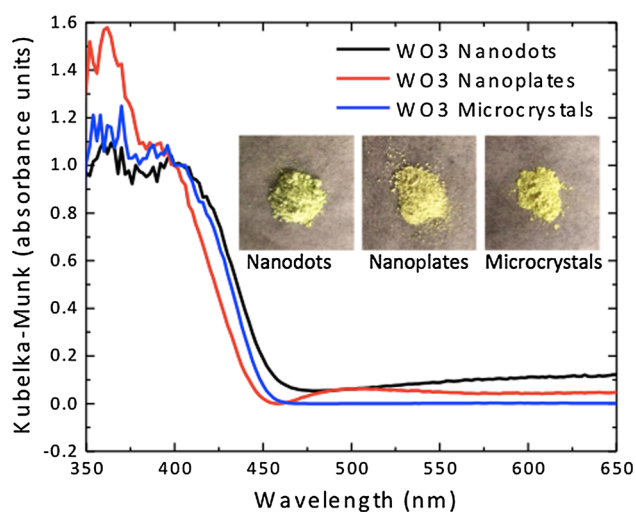


Fig. 2 Kubelka–Munk absorbance with photographs of the three types of WO_3 samples

and $2.9 \mu\text{mol h}^{-1}$ for the microcrystals. The low evolution rate for the microcrystals is close to the background evolution from just NaIO_4 , making the assignment of a photocatalytic reaction ambiguous in this case. Oxygen evolution rates and other data are summarized in Table 1.

Interestingly, a plot of the O_2 evolution rate versus the *inverse* particle diameter is nearly linear (Fig. 3b). This suggests the O_2 evolution activity of the crystals is limited by minority carrier transport within WO_3 (see further discussion below).

To evaluate the photoelectrochemical properties of the different WO_3 particles, electrochemical scans were conducted on WO_3 films on FTO immersed in 0.1 M aqueous K_2SO_4 at pH 3.5, with or without added methanol (Fig. 4). Photoanodic currents in the absence of methanol (Fig. 4a) are mainly attributed to the oxidation of water, with some persulfate formation occurring also [7, 30, 44]. Currents are generally below $30 \mu\text{A cm}^{-2}$ and increase as particle size decreases. In contrast, the photoonset potentials near $+0.25 \text{ V}$ versus NHE vary little with particle size. Scans performed under LED illumination at 435 nm (Fig. S5) allow calculation of the Incident Photon-to Current Efficiency (IPCE) values. The values are $5.45 \times 10^{-4} \%$, $3.32 \times 10^{-4} \%$, and $3.12 \times 10^{-5} \%$ for nanodots, nanoplates, and microcrystals, respectively. This shows that at $+1.0 \text{ V}$ applied potential, the photooxidation ability of the WO_3 particles is mainly limited by e^-/h^+ recombination. The situation improves in the presence of methanol as sacrificial electron donor (Fig. 4b).

Photocurrents increase by factors of 50, 13, and 6 for nanodots, nanoplates, and microcrystals, respectively, while photoonsets are shifted by $\sim 150 \text{ mV}$ toward reducing potential. These changes are brought about by faster hole charge transfer into the liquid phase caused by

the lower oxidation potential of methanol compared to water. The energetics of photocatalytic water and methanol oxidation with WO_3 are described in the energy scheme in Fig. 5. A single scheme is adequate for the three types of WO_3 particles in this study because the quasi-Fermi electron levels (from photoionization potentials in aqueous

methanol, see Table 1) are similar across the series, and variations in the band gap are not significant. The thermodynamics of charge separation are the same for all three sizes of WO_3 ; thus, any observed differences in the photocatalytic activity are a result of kinetic effects. These differences can be understood quantitatively in terms of the one dimensional continuum model in Fig. 6 [34, 35]. According to this model, the photocatalytic rate of WO_3 is controlled by the rates of charge generation, charge recombination, and charge transfer to the redox species on the particle surface. Analytically, this is expressed as Eq. 1 for the overall catalytic rate ER (moles of transferred electrons per particle volume and time) of the WO_3 particles.

$$ER \left[\frac{\text{mol}}{\text{cm}^3 \text{s}} \right] = \left(\frac{1}{R_G - R_R^L - R_R^S} + \frac{r}{J_{CT}^-} + \frac{r}{J_{CT}^+} + \frac{1}{R_{OX} S_{OX}} + \frac{1}{R_{RED} S_{RED}} \right)^{-1} \quad (1)$$

In Eq. 1, ER is calculated as the inverse of the sum of the inverse rates for charge generation (R_G) and recombination (R_R), charge transfer (J_{CT}), and redox reactions (R_{REDOX}). This is analogous to the overall conductance of a series of conductances, according to Kirchhoff's law. Under these conditions, ER is determined by the smallest rate in the series. For example, if charge transport to the surface (J_{CT}^+ , J_{CT}^-) is rate limiting, Eq. 1 transforms into Eq. 2.

$$ER \left[\frac{\text{mol}}{\text{cm}^3 \text{s}} \right] = \left(\frac{r}{J_{CT}^-} + \frac{r}{J_{CT}^+} + \text{small constant} \right)^{-1} \quad (2)$$

This model describes the size trends of the photocatalytic activity of WO_3 well. A linear relation between ER and the inverse particle radius (diameter) is clearly observed in the data in Figs. 3b, 4c. For photocatalytic or photoelectrochemical *water oxidation*, the short nanoplate diameter (58 nm) fits the plots better than the *average* plate diameter (235 nm). This indicates that the redox reactions occur predominantly on the flat faces of the plates, to which photochemical charge transfer is the fastest. Based on the published effective masses of electrons ($0.9 m_e$) and holes ($2.0 m_e$) in WO_3 [46], electron diffusion is faster than

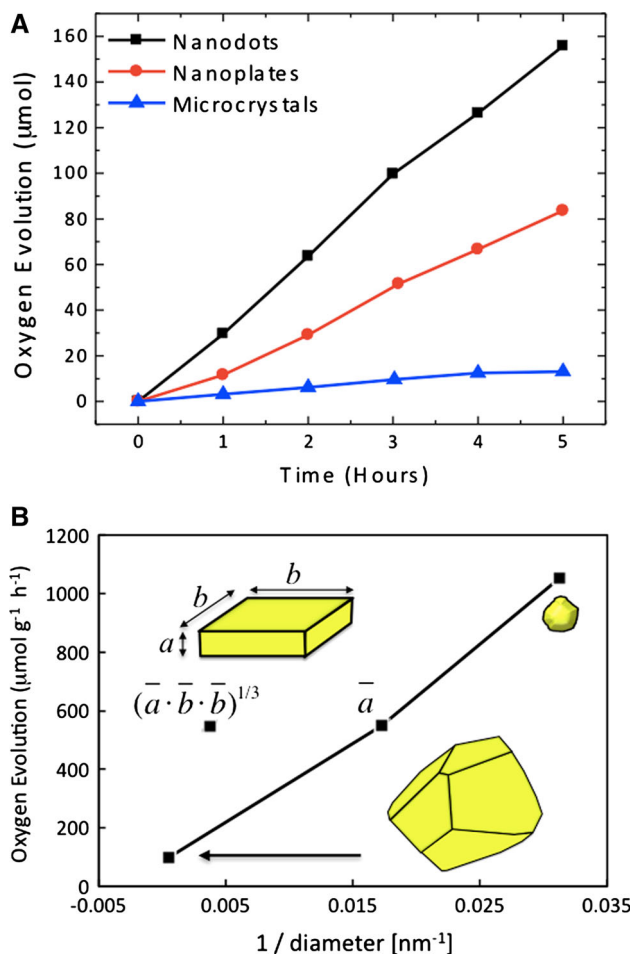


Fig. 3 **a** Oxygen evolution using 30 mg of catalyst in 80 mL of 0.01 M NaIO_4 solution at pH 3.5. The light (>400 nm, 610 mW cm^{-2} at the flask surface) was generated by a 300 W Xe lamp and passed through a 0.22 M aqueous NaNO_2 solution filter. **b** O_2 evolution rates versus inverse average particle size. For the nanoplates, both the shortest and the averaged (geometric) dimensions are plotted

Table 1 Selected properties of WO_3 particles

Particle size	Particle dimensions (nm)	Band gap, E_G (eV)	E_{Fn} (V vs. NHE) ^a	O_2 evolution ($\mu\text{mol h}^{-1} \text{g}^{-1}$)	Photocurrent (at 1.0 V in water) (μA)	IPCE at 435 nm and +1.0 V (%) ^a	Photocurrent (at +1.0 V in aq. CH_3OH) (mA) ^a
Nanodots	32 ± 16	2.75	0.112	31.63	25.0	5.45×10^{-4}	1.32
Nanoplates	$475 \pm 98, 58 \pm 16$	2.87	0.091	16.48	17.8	3.32×10^{-4}	0.24
Microcrystals	~ 2000	2.80	0.076	2.9	7.7	3.12×10^{-5}	0.048

^a In aqueous 0.1 M K_2SO_4 at pH 3.5

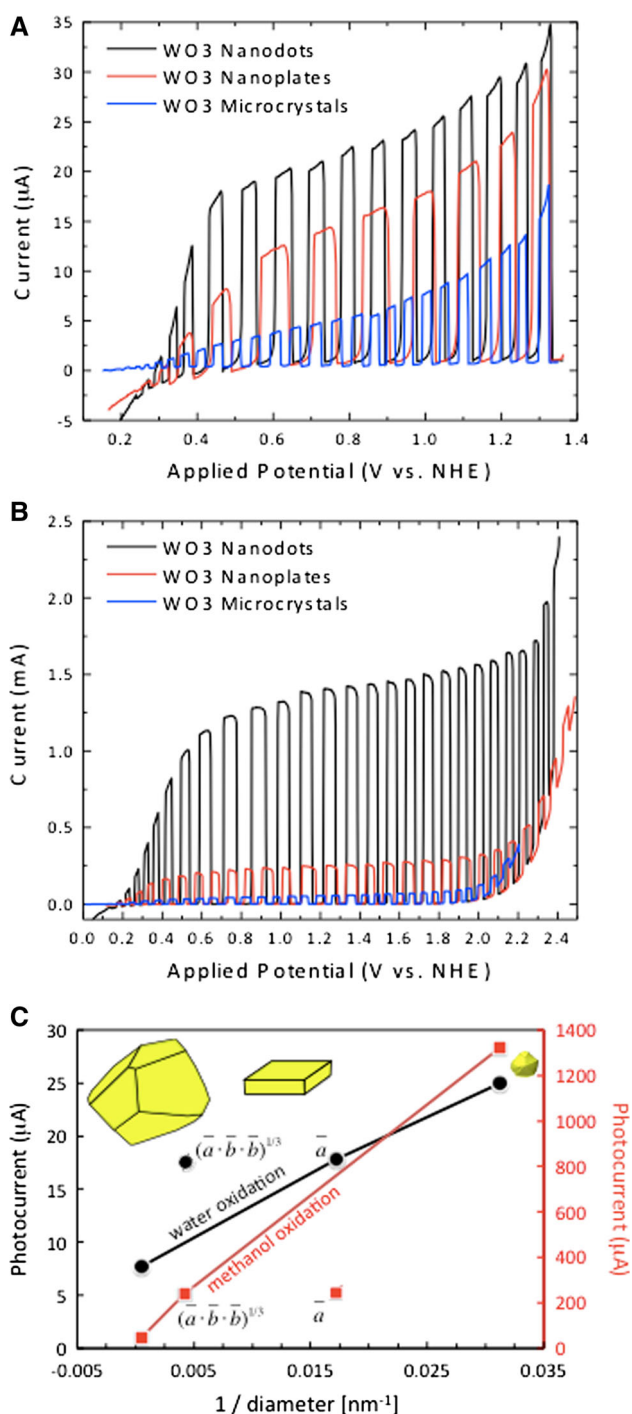


Fig. 4 Photoelectrochemical chopped light scans of WO_3 on FTO illuminated by Xe lamp (45 mW cm^{-2}) in **a** water or in **b** 20 % (v:v) aqueous methanol. Supporting electrolyte was 0.1 M K_2SO_4 at pH 3.5. **c** Photocurrent versus inverse particle size (two values for nanoplates)

hole diffusion. This means the τ/J_{CT}^+ term will dominate in Eq. 2. The situation changes when methanol is added to the electrolyte. Now a straight line in the current versus inverse size plot in Fig. 4c is observed only if the *average* diameter of the nanoplates is used instead of the *short* diameter. This is because with methanol, the faster redox reagent, the

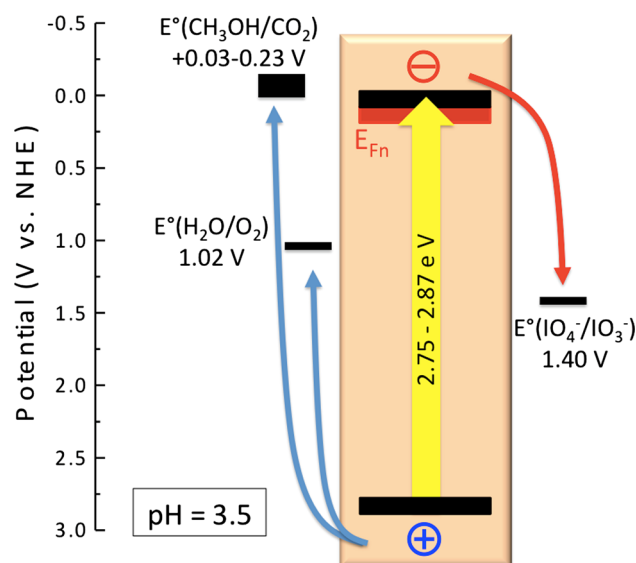


Fig. 5 Representative energy scheme for all WO_3 particles at pH 3.5 with electrochemical potentials for selected redox couples [42, 45]

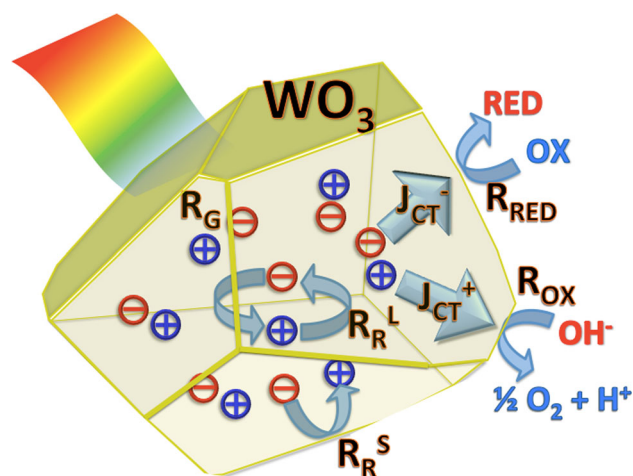


Fig. 6 Charge generation (R_G), recombination (R_R), transfer (J_{CT}), and redox (R_{REDOX}) pathways in illuminated WO_3 particles of radius r , volume V , and surface S in contact with water. S_{RED} and S_{OX} (not shown) are the active surfaces areas for reduction and oxidation, respectively. R_R^L and R_R^S correspond to lattice and surface recombination, respectively

photocurrent also increasingly depends on majority charge carrier (electron) transport J_{CT}^- through the films [30]. Under these circumstances longer particle dimensions are advantageous over small ones, because they offer a more continuous electron transport path through the film.

4 Conclusion

We have shown that under strong applied bias, the photocatalytic and photoelectrochemical properties of WO_3 crystals in the 32–2000 nm size range are controlled by the

kinetics of charge transfer. For the slow water oxidation reaction, photochemical hole transport to the particle surface is rate limiting. For the faster methanol oxidation reaction, both photochemical hole transport to the particle surface and electron transport through the WO_3 film are rate limiting. These observations can be quantitatively understood with the one-dimensional continuity model for charge generation, recombination, and transport. This study sheds light on the factors that determine photochemical charge separation in particle-based light absorbers. It will help design more efficient systems for solar energy to fuel conversion.

Acknowledgments We thank Jing Zhao for SEM images and Joshua Greenfield and Kirill Kovnir for XRD data and Adam Moulé for access to the profilometer. We are grateful for financial support from Research Corporation for Science Advancement (Sciolog Award) and from the National Science Foundation (NSF, Grants 1152250 and 1133099).

References

- Osterloh FE (2008) *Chem Mater* 20:35–54
- Osterloh FE (2013) *Chem Soc Rev* 42:2294–2320
- Osterloh FE (2015) *Top Curr Chem* 371:105–142
- Hodes G, Cahen D, Manassen J (1976) *Nature* 260:312–313
- Di Quarto F, Di Paola A, Sunseri C (1981) *Electrochim Acta* 26:1177–1184
- Smestad GP, Krebs FC, Lampert CM, Granqvist CG, Chopra KL, Mathew X, Takakura H (2008) *Sol Energy Mater Sol Cells* 92:371–373
- Mi Q, Zhanaidarova A, Brunschwig BS, Gray HB, Lewis NS (2012) *Energy Environ Sci* 5:5694–5700
- Vidyarthi VS, Hofmann M, Savan A, Sliozberg K, König D, Beranek R, Schuhmann W, Ludwig A (2011) *Int J Hydrogen Energy* 36:4724–4731
- Waller M, Townsend TK, Zhao J, Sabio EM, Chamousis RL, Browning ND, Osterloh FE (2012) *Chem Mater* 24:698–704
- Santato C, Ulmann M, Augustynski J (2001) *J Phys Chem B* 105:936–940
- Santato C, Odziemkowski M, Ulmann M, Augustynski J (2001) *J Am Chem Soc* 123:10639–10649
- Santato C, Ulmann M, Augustynski J (2001) *Adv Mater* 13:511–514
- Bignozzi CA, Caramori S, Cristino V, Argazzi R, Meda L, Tacca A (2013) *Chem Soc Rev* 42:2228–2246
- Abe R, Takata T, Sugihara H, Domen K (2005) *Chem Commun* 30:3829–3831
- Ma SSK, Maeda K, Abe R, Domen K (2012) *Energy Environ Sci* 5:8390–8397
- Ma SSK, Maeda K, Hisatomi T, Tabata M, Kudo A, Domen K (2013) *Chem Eur J* 19:7480–7486
- Maeda K, Higashi M, Lu D, Abe R, Domen K (2010) *J Am Chem Soc* 132:5858–5868
- Kato H, Sasaki Y, Iwase A, Kudo A (2007) *Bull Chem Soc Jpn* 80:2457–2464
- Sasaki Y, Nemoto H, Saito K, Kudo A (2009) *J Phys Chem C* 113:17536–17542
- Solarska R, Alexander BD, Braun A, Jurczakowski R, Fortunato G, Stiefel M, Graule T, Augustynski J (2010) *Electrochim Acta* 55:7780–7787
- Pesci FM, Cowan AJ, Alexander BD, Durrant JR, Klug DR (2011) *J Phys Chem Lett* 2:1900–1903
- Seabold JA, Choi KS (2011) *Chem Mater* 23:1105–1112
- Qin DD, Tao CL, Friesen SA, Wang TH, Varghese OK, Bao NZ, Yang ZY, Mallouk TE, Grimes CA (2012) *Chem Commun* 48:729–731
- Amano F, Li D, Ohtani B (2011) *J Electrochem Soc* 158:K42–K46
- Chakrapani V, Thangala J, Sunkara MK (2009) *Int J Hydrogen Energy* 34:9050–9059
- Sabio EM, Chamousis RL, Browning ND, Osterloh FE (2012) *J Phys Chem C* 116:3161–3170
- Townsend TK, Sabio EM, Browning ND, Osterloh FE (2011) *Energy Environ Sci* 4:4270–4275
- Chamousis RL, Osterloh FE (2014) *Energy Environ Sci* 7:736–743
- Solarska R, Jurczakowski R, Augustynski J (2012) *Nanoscale* 4:1553–1556
- Zhao J, Olide E, Osterloh FE (2015) *J Electrochem Soc* 162:H65–H71
- Darwent JR, Mills A (1982) *J Chem Soc Faraday Trans II* 78:359–367
- Hong SJ, Jun H, Borse PH, Lee JS (2009) *Int J Hydrogen Energy* 34:3234–3242
- Amano F, Ishinaga E, Yamakata A (2013) *J Phys Chem C* 117:22584–22590
- Sabio EM, Chamousis RL, Browning ND, Osterloh FE (2012) *J Phys Chem C* 116:19051
- Sabio EM, Chamousis RL, Browning ND, Osterloh FE (2012) *J Phys Chem C* 116:3161–3170
- Richardson E (1959) *J Inorg Nucl Chem* 12:79–83
- Choi Y-G, Sakai G, Shimanoe K, Miura N, Yamazoe N (2002) *Sens Actuators B* 87:63–72
- Amano F, Ishinaga E, Yamakata A (2013) *J Phys Chem C* 117:22584–22590
- Santato C, Ulmann M, Augustynski J (2001) *J Phys Chem B* 105:936–940
- Solarska R, Santato C, Jorand-Sartoretti C, Ulmann M, Augustynski J (2005) *J Appl Electrochem* 35:715–721
- Waller MR, Townsend TK, Zhao J, Sabio EM, Chamousis RL, Browning ND, Osterloh FE (2012) *Chem Mater* 24:698–704
- Vanysek P (2008) In: *CRC handbook of chemistry and physics*, 88th edn. CRC Press, Boca Raton (Internet Version 2008)
- Sayama K, Mukasa K, Abe R, Abe Y, Arakawa H (2002) *J Photochem Photobiol A* 148:71–77
- Hill JC, Choi K-S (2012) *J Phys Chem C* 116:7612–7620
- Burstein GT, Barnett CJ, Kucernak AR, Williams KR (1997) *Catal Today* 38:425–437
- Berak JM, Sienko MJ (1970) *J Solid State Chem* 2:109–133